In-situ structural and electrical conductivity characterization of $Sr_2MMoO_{6-\delta}$ double perovskite solid oxide fuel cell anode materials

Journal:	*ACS Applied Energy Materials*
Manuscript ID	ae-2020-003763.R2
Manuscript Type:	Article
Date Submitted by the Author:	08-May-2020
Complete List of Authors:	Witt, Suzanne; National Institute of Standards and Technology, Material Measurement Laboratory; Fraunhofer USA, Center for Coatings and Diamond Technologies Allen, Andrew; National Institute of Standards and Technology, Material Measurement Laboratory Kuzmenko, Ivan; Argonne National Laboratory, X-ray Science Division Holtz, Megan; National Institute of Standards and Technology, Material Measurement Laboratory Young, Sandra; National Institute of Standards and Technology, Material Measurement Laboratory

In-situ structural and electrical conductivity characterization of $Sr_2MMoO_{6-\delta}$ double perovskite solid oxide fuel cell anode materials

Suzanne E. Witt[a,,§], Andrew J. Allen[a], Ivan Kuzmenko[b], Megan E. Holtz[a], Sandra Young[a]*

[a]Material Measurement Laboratory, National Institute of Standards and Technology (NIST), Gaithersburg, MD 20899, USA

[b]X-ray Science Division, Advanced Photon Source, Argonne National Laboratory, Argonne, IL 60439, USA

ABSTRACT

In this study, a series of $Sr_2MMoO_{6-\delta}$ double perovskite solid oxide fuel cell (SOFC) anode materials (where $0 \leq \delta \leq 0.041$ and M = Fe, Co, or Ni) were synthesized, and the changes in their morphologies under relevant SOFC operating conditions were explored. Ultra-small-angle X-ray scattering (USAXS), small-angle X-ray scattering (SAXS) and wide-angle X-ray scattering (WAXS) were used to determine changes in the microstructures and phase compositions of the anode materials at high temperature and under reducing atmosphere. The stability of the double perovskite structure was found to be highly dependent on the identity of the cation M, such that when M = Fe, the material remained stable over the course of the experiments. However, when M

= Co or Ni, significant changes in the microstructure and phase composition were observed. An *in-situ* study of the *M* = Co sample, in which electrical conductivity and USAXS/SAXS/WAXS measurements were conducted simultaneously, revealed the structural degradation mechanisms and electrical conductivity changes over a range of temperatures. To conduct these measurements, a cell was developed that allowed for a sample mounted on Pt wire to be placed in the X-ray beam and heated under gas flow comprising 4 % mass H_2 and 96 % mass N_2. The resulting measurements allowed for the direct comparison of the electrical and morphological changes occurring in the material under operating conditions, such that increases in conductivity could be attributed to the growth of new phases.

KEYWORDS

solid oxide fuel cells, X-ray scattering, *in-situ* technique, conductivity, double perovskite

INTRODUCTION

Solid oxide fuel cells (SOFCs) are a promising energy technology that function by converting chemical energy to electricity at high temperatures. High efficiencies and power densities, fuel flexibility, and lower emissions compared to traditional energy conversion systems are some advantages unique to SOFCs that continue to spur interest in their development. An SOFC consists of a porous anode and cathode separated by a dense solid electrolyte. Fuel oxidation occurs within the anode, and oxygen reduction within the cathode completes the circuit to drive a current between the electrodes while protons or oxygen ions flow through the electrolyte. Traditional SOFCs operate at temperatures near 1000 °C to achieve optimal oxygen ion conductivity in yttria-stabilized zirconia (YSZ), a common electrolyte material.[1] However, material degradation and high operating costs drive efforts to lower SOFC operating temperatures to an intermediate range

(500 °C to 800 °C).[1,2] Therefore, materials that operate effectively under such conditions while maintaining their structural integrity are of interest for next-generation SOFCs.

Typical SOFC anode materials, such as Ni-YSZ composites, contain Ni to catalyze the reduction of H_2 fuel due to its high electrocatalytic activity and low cost.[2] However, the presence of Ni poses a number of issues, such as carbon deposition and sulfur poisoning, that negatively impact cell performance due to degradation of the anode.[2] Therefore, alternatives to Ni-YSZ are currently being investigated. One promising class of materials is double perovskites. These compounds have the general formula $A_2B'B''O_{6-\delta}$ with multivalent metal ions in the octahedrally coordinated B positions, which allow for high electrical conductivities.[3] Several double perovskite compounds have exhibited properties that are desirable for SOFC electrode materials, such as chemical stability under either oxidizing or reducing conditions, or a high resistance to carbon deposition or sulfur poisoning.[2] In 2006, a series of $Sr_2Mg_{1-x}Mn_xMoO_{6-\delta}$ double perovskite compounds were used as SOFC anodes for the first time. They exhibited resistance to sulfur poisoning and high power outputs when exposed to fuel gasses at high temperatures.[4] Since then, the use of $Sr_2MgMoO_{6-\delta}$ compounds as anodes has been explored extensively,[5–8] and the study of similar materials as anodes has expanded to include $Sr_{1.9}VMoO_{6-\delta}$,[9] $Sr_2Fe_{1.5}Mo_{0.5}O_{6-\delta}$,[5,10] $Sr_2FeMoO_{6-\delta}$,[11–13] $Sr_2CoMoO_{6-\delta}$,[5,14–16] and $Sr_2NiMoO_{6-\delta}$.[5,14,15,17–19] The stability of these materials under SOFC operating conditions has been repeatedly shown to be dependent on their composition, particularly the identity of the B' site cation, and is typically evaluated through *ex-situ* measurements before and after operation. This limits the analysis of morphology and phase changes in the anode materials to the initial and final states, and does not capture the step-wise decomposition processes occurring in the material during operation.

To evaluate the feasibility of these new materials as SOFC anodes, a means to study their interaction with the fuel gas *in-operando* is required. Several electrical cells have previously been constructed for use in combination with various X-ray techniques, but none of these stages are suitable for measurements at SOFC operating temperatures.[20–31] In this work, an electrical cell was developed to simultaneously collect *in-situ* ultra-small-angle X-ray scattering (USAXS), small-angle X-ray scattering (SAXS), wide-angle X-ray scattering (WAXS), and electrical conductivity measurements on a series of double perovskite anode materials under relevant SOFC operating temperatures and gas environments.

EXPERIMENTAL

SMMO synthesis and sample preparation

$Sr_2MMoO_{6-\delta}$ (S*M*MO, where $0 \leq \delta \leq 0.041$[32] and *M* = Fe, Co, Ni) samples were synthesized *via* conventional solid-state reactions. The samples are referred to herein as SFMO when *M* = Fe, SCMO when *M* = Co and SNMO when *M* = Ni. $SrCO_3$ (99.994 %) and MoO_3 (99.5 %) were combined with Fe_2O_3 (99.0 %), CoO (99.995 %) or NiO (99.9 %) precursor powders in stoichiometric ratios (2 mol Sr^{II} : 1 mol $M^{III/II}$: 1 mol Mo^{VI}), mixed with ethanol to form a slurry, and then ball-milled for ≈ 30 min. The resulting mixture was dried on a hot plate, then ground to a fine powder using a mortar and pestle. SFMO was sintered under forming gas (5 % mass H_2 / 95 % mass N_2) at 1100 °C for 10 h, while SCMO and SNMO were sintered at 1250 °C for 10 h in air.[3] SCMO was further treated at 800 °C for 2 h under forming gas to obtain a single phase.[16] The XRD patterns for each sample showed the desired, pure phase.

For *in-situ* measurements, SCMO pellets were formed by first mixing the dry powder with a 10 % mass Paraloid† (Dow Chemical Co., Midland, MI) binder in acetone. The powder/binder mixture was pressed into ≈ 4 mm × 5 mm pellets using a rectangular die. The pellets were polished to ≈

100 μm in thickness using a diamond polishing wheel, then heated at 750 °C for 48 h in air to densify the pellet while maintaining planarity. Thin pellets were required to minimize X-ray beam attenuation due to absorption in the sample. The final pellet dimensions after heating were 3.50 ± 0.02 mm × 4.50 ± 0.02 mm. With the pellets mounted vertically in the X-ray beam and ≈ 100 μm thickness, the porosity was found to be ≈ 15 %, as determined from the X-ray scattering measurements described below.

X-ray electrical cell assembly

The electrical cell was assembled by feeding two Pt electrical wires through double-bore alumina tubing. The wires were secured at each end with OMEGABOND "700" High Temperature Chemical Set Cement (Omega Engineering, Inc., Norwalk, CT, USA). This assembly was then cured at ambient temperature before proceeding to the next step, in which the rectangular SCMO pellets described above were attached to the Pt wires using H22 Epo-Tek Silver Conductive Epoxy (Ted Pella, Inc. Redding, CA, USA). Both wires were attached to one face of the pellet, with one wire near what would become the top edge of the vertically-mounted sample in the X-ray beam (above the beam) and the other wire near what would become the bottom edge (below the X-ray beam), see Figure S1. This was in order to apply a DC voltage across the length (height in the X-ray beam) of the pellet during conductivity measurements. The entire cell assembly was then heated at 750 °C for 6 h under nitrogen to ensure a strong bond between all components.

To perform *in-situ* X-ray and electrical conductivity measurements, a cell was placed inside a 75 mm long rectangular quartz capillary (1 mm wall thickness) which was suspended between two Thorlabs (Thorlabs, Inc., Newton, NJ, USA) plates (for an image of the cell assembly, see the Supporting Information). A thermocouple was placed inside one end of the capillary to measure the cell temperature. Forming gas (4 % mass H_2 / 96 % mass N_2[‡]) also flowed through this opening.

The other end of the assembly contained the gas outlet and a Swagelok (Swagelok Company, Solon, OH, USA) connector, through which the alumina tubing holding the electrical wires was inserted. The Pt wires extended beyond the edge of this plate and were connected to a Keysight B2901A Precision Source/Measure Unit (Keysight Technologies, Santa Rosa, CA, USA), which was used to measure electrical conductivity during the experiment.

To heat the sample, two sets of coils made of 0.644 mm diameter (22 gauge) Kanthal A1 resistance wire (RBA Depot, Rowland Heights, CA, USA) were mounted in close proximity to the quartz capillary, external to the sample. A current was passed through the coils to supply heat and bring the sample to the desired temperature, which was measured by the thermocouple inside the capillary next to the sample. The entire assembly was set up for measurements using the X-ray beamline at Sector 9-ID of the Advanced Photon Source (APS), Argonne National Laboratory, Argonne, IL, USA (APS USAXS facility). The current state of development of the APS USAXS facility is described in detail elsewhere.[33] Using primary calibration methods, this facility provides absolute-intensity calibrated scattering intensity, $I(q)$,as a function of q ($q = (4\pi/\lambda)\sin\theta$, where λ is the X-ray wavelength and θ is one half of the scattering angle). Due to the crystal diffraction optics that underlies the USAXS setup, USAXS data are intrinsically slit-smeared. While the data can be de-smeared, this introduces noise artifacts into the data. Thus, it is usually appropriate to slit-smear the SAXS data before merging with USAXS, and model-fit to the combined slit-smeared data, as has been done here. USAXS measurements have been used previously in the characterization of SOFC materials and degradation issues.[34,35] Here, USAXS/SAXS/WAXS were collected every ≈ 5 min while current-voltage (IV) curves were measured simultaneously as the sample was slowly heated from room temperature to 825 °C. IV curves were generated by applying a range of DC voltages across the length of the sample, measuring the output current

values and then plotting these as a function of the applied voltage for each temperature. The resistance (R) of the sample at each temperature was determined from the inverse of the linear slope of the IV curves, which was converted to resistivity (ρ) using the following relationship:

$$\rho = R \times \frac{A}{l}$$

where A is the sample area (15.75 ± 0.16 mm^2) and l is the sample length (3.50 ± 0.02 mm). The conductivity of the sample was then calculated by taking the reciprocal of ρ and is plotted as a function of temperature (see later discussion).

Modeling X-ray scattering data

Size distributions and volume fractions (VFs) of the scattering features were determined by assuming multi-component lognormal VF size distributions and fitting the predicted scattering profile to the combined USAXS/SAXS data, $I(q)$ *versus* q, measured for 0.001 nm^{-1} < q < 15 nm^{-1}.[36] The data were fit using a two-population model, from which the mean diameter (MD) and VF of each population were calculated. The VFs of population 1 were estimated assuming an X-ray scattering contrast factor between the pores (zero density) and the surrounding solid medium. The X-ray form-factor density of the latter was corrected for changes in composition of the crystalline phases present, based on analysis of the XRD patterns (Table S1 and Figure S2). For population 2, the average contrast between Co and the surrounding solid medium (850 x 10^{20} cm^{-4}) was used. The fitting was accomplished using the *Irena* macros which are integrated with the USAXS facility data reduction and analysis routines written in *Igor Pro* (Wavemetrics, Lake Oswego, OR, USA) software.[36] Approximate phase fractions were calculated by least squares fitting of the diffraction peak patterns in the WAXS data (measured as $I(q)$ *versus* q in the range 15 nm^{-1} < q < 70 nm^{-1}) using publicly-available *GSAS-II* software.[37] Scanning electron microscopy (SEM) was performed

on the initial and heat-treated SCMO samples to validate the proposed size-distribution and VF models (Helios NanoLab DualBeam microscope, ThermoFisher Scientific, Waltham, MA, USA).

RESULTS & DISCUSSION

Ex-situ USAXS/SAXS/WAXS

The S*M*MO powders were heated at 1000 °C for one hour under 4 % mass H_2 / 96 % mass N_2 (forming gas). USAXS/SAXS/WAXS measurements were collected on the as-synthesized powders and after the heat treatment (Figure 1). The combined USAXS/SAXS profiles (Figure 1 a-c) indicate that the SFMO powder retained its initial morphology after the heat treatment, but the growth of a new scattering feature was observed for SCMO and SNMO. When fitting the USAXS/SAXS data, this new feature can be assigned to the growth of a new population of Co or Ni nanoparticles due to their exsolution from the SCMO and SNMO structures, respectively.[5,14,15,17,38] This is corroborated by the WAXS data, which reveal no new phases after the heat treatment of SFMO (but does show significant peak broadening, indicating a possible decrease in grain size), whereas a reduction of the initial phase (labeled A in Figure 1 d-f) and growth of product phases is observed in both SCMO and SNMO. The new phases are identified as $SrMoO_4$, $SrMoO_3$, and Sr_3MoO_6 (labeled B, C, D in Figure 1 d-f, respectively).[5,14,15,17,38,39] Due to the increased sensitivity of the WAXS measurements, trace amounts of an impurity are observed in the initial profiles for SCMO and SNMO that were not seen in the XRD profiles of the as-synthesized powders. This is likely the $SrMoO_4$ phase that grows in upon heating the sample. Peaks for Co or Ni nanoparticles could not be detected presumably because they were too broad (due to the small particle size) and overlapped with those of the strontium molybdate phases. However, the exsolution of Co or Ni is required for the formation of the observed Sr_3MoO_6 phase.

Therefore, the chemical reduction of SCMO and SNMO at high temperatures can be described by Equation 1[40]:

$$4Sr_2MMoO_6 \xrightarrow{\Delta,\ H_2} 2Sr_3MoO_6 + SrMoO_4 + SrMoO_3 + 4M + \frac{5}{2}O_2\ , \qquad (1)$$

where M = Co or Ni. The exsolution of M coincides with the formation of the double perovskite Sr_3MoO_6, which may be re-written as Sr_2SrMoO_6, and the scheelite-type $SrMoO_4$ and single perovskite $SrMoO_3$ phases[5,8].

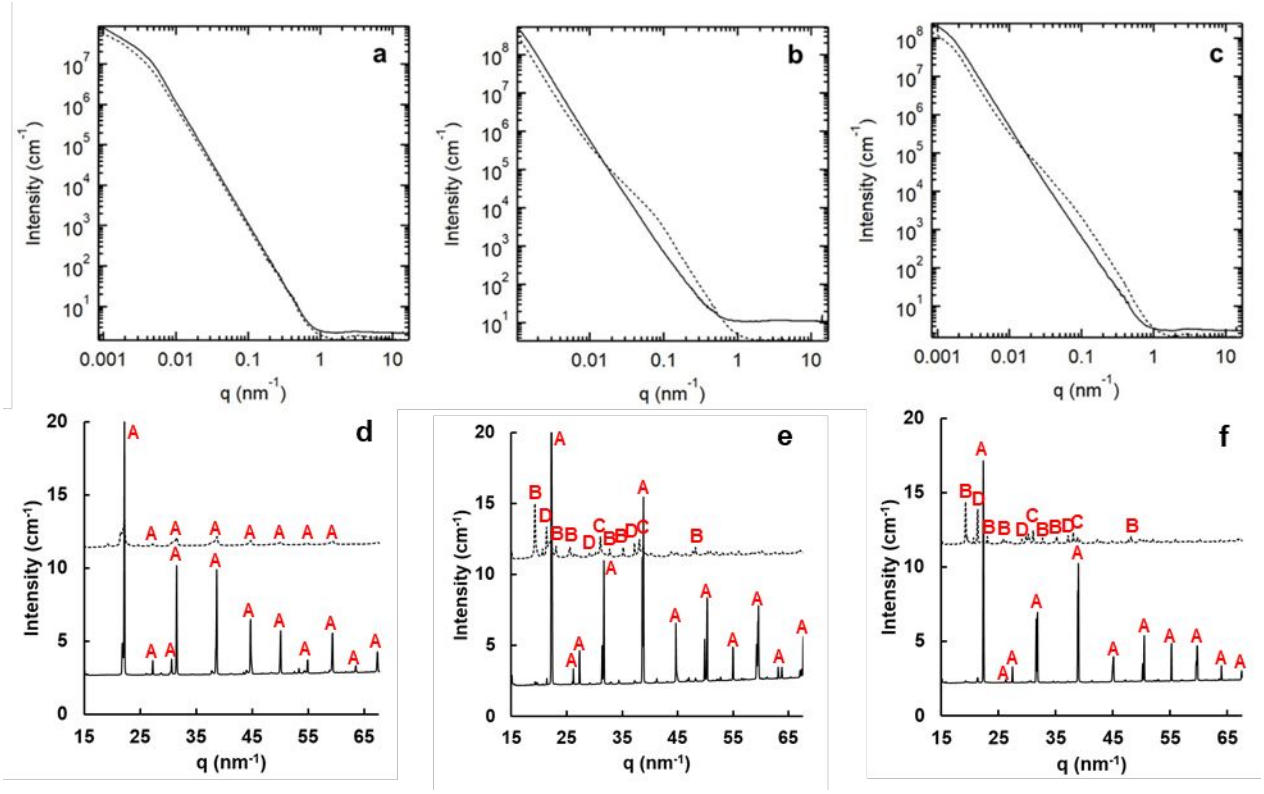

Figure 1. X-ray scattering profiles of the S*M*MO samples before (solid lines) and after (dashed lines) heat treatment at 1000 °C under 4 % mass H_2 / 96 % mass N_2 atmosphere for 1 h. Top: log-log plots of combined slit-smeared USAXS/SAXS absolute intensity, $I(q)$ *versus* q for SFMO (a), SCMO (b) and SNMO (c). Bottom: linear-linear plots of WAXS intensity *versus* q for SFMO (d), SCMO (e) and SNMO (f) showing XRD patterns (Sr_2MMoO_6 (A), $SrMoO_4$ (B), $SrMoO_3$ (C),

Sr_3MoO_6 (D)). The patterns collected after heat treatment are shifted vertically in the plots. Point-to-point data uncertainties are smaller than data point symbols in the plots.

The differences in stability of the three compounds during heating under reducing conditions is dependent on the cation *M* and the ease with which *M* can be reduced from a positively charged ion to a neutral metal atom. In SFMO, Fe ions likely exist in a mixed Fe^{III}/Fe^{II} oxidation state, while Mo exists as a Mo^{VI}/Mo^{V} mixture.[32,41–44] Overlap of the $Fe^{III/II}$ and $Mo^{VI/V}$ redox energies results in stabilization of the Fe oxidation state under reducing conditions, and therefore enhanced stability at high temperatures.[32] In contrast, Co and Ni in the as-synthesized SCMO and SNMO, respectively, are both likely to exist as 2+ ions. Insufficient overlap of the $Co^{III/II}$ and $Ni^{III/II}$ redox energies with $Mo^{VI/V}$ leads to the full reduction of these metal ions to M^0 and their subsequent exsolution under these gas conditions.[5,14,15,17,38]

In-situ USAXS/SAXS/WAXS

To further probe the reactivity of the S*M*MO double perovskite anode materials under relevant SOFC conditions, an *in-situ* study was conducted using the SCMO sample. The mounted sample (described in the Experimental section) was slowly heated to 825 °C under a flow of 4 % mass H_2 / 96 % mass N_2 gas while USAXS/SAXS/WAXS, and current-voltage (I-V) data were collected. Data collected below 400 °C has been omitted for clarity, as no changes in the X-ray scattering profiles were detected in this regime.

The combined USAXS/SAXS data for the *in-situ* experiment are shown in Figure 2. Like the *ex-situ* data, the growth of a new population at intermediate *q* values is observed. At the same time, there is a reduction in the scattering intensity at low *q*. The VFs and MDs calculated from fitting the data (as described in the Experimental section) are plotted as a function of temperature in Figure 3. The modeling results indicate that for population 1, which corresponds to the features

that scatter at low q values, the VF decreases from ≈ 15 % of the total sample volume to a final value of ≈ 10 %, with minor fluctuations in between (Figure 3a, blue line). For population 2, which corresponds to features that dominate the scattering at intermediate q values, the VF steadily increases from an initial value of 0.82 % to a final value of 6.1 % of the sample volume (Figure 3b, blue line). The MD of population 1 is initially ≈ 550 nm, then increases to a maximum of 576 nm between 535 °C and 576 °C, at which point it decreases to 520 nm at 697 °C (Figure 3a, red line). Between 697 °C and 755 °C, the MD of population 1 increases again to 537 nm, then decreases as the temperature increases, reaching a final value of 464 nm. For population 2, the MD steadily decreases from an initial value of 7.1 nm to 5.1 nm at 542 °C, then increases to a maximum of 8.7 nm at 642 °C (Figure 3b, red line). Between 642 °C and 723 °C, the MD of population 2 decreases to 5.6 nm, then sharply increases with temperature to reach a final value of 17 nm. To understand the results of the USAXS/SAXS modeling, one can look at the phase changes as a function of temperature in the WAXS data.

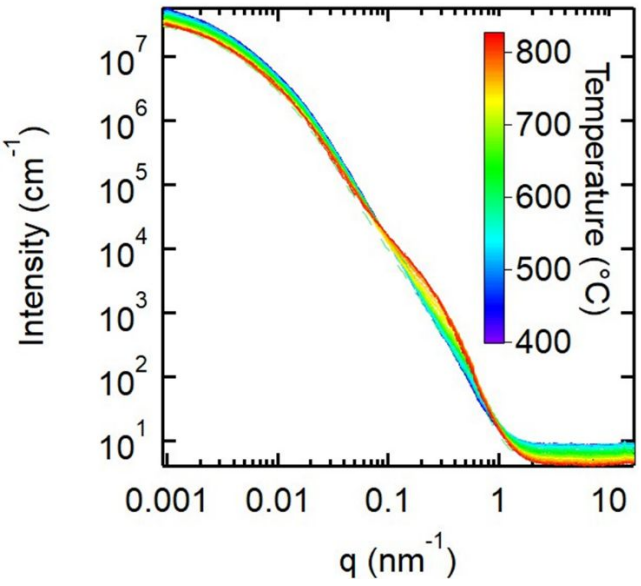

Figure 2. *In-situ* slit-smeared USAXS/SAXS of SCMO collected from 400 °C to 825 °C under a flow of 4 % mass H_2 / 96 % mass N_2 gas. Statistical uncertainties are smaller than the line thicknesses plotted.

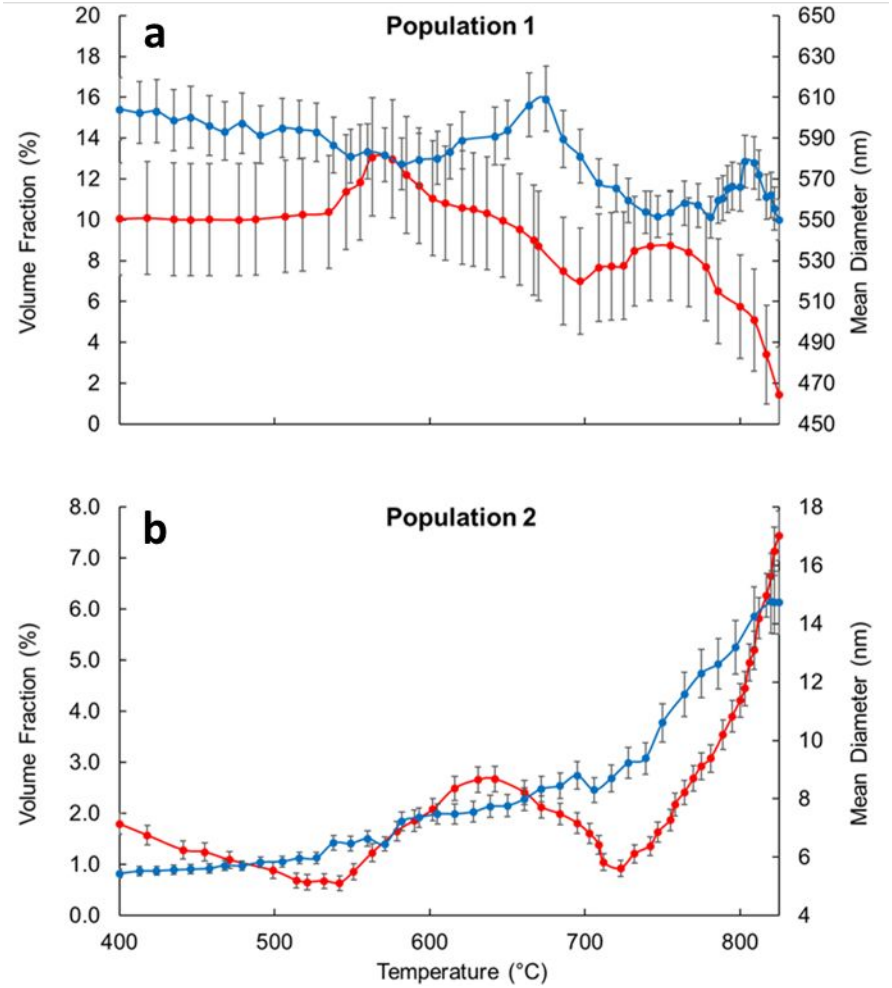

Figure 3. Model-fit VFs (blue lines) and MDs (red lines) of the scattering features as a function of temperature for population 1 (a) and population 2 (b). Estimated uncertainties in the VFs and MDs for both populations are ± 10 % and ± 5 %, respectively.

The *in-situ* WAXS data are shown in Figure 4. Due to the longer reaction time (≈ 13.5 h *versus* 1 h), the *in-situ* experiment revealed the formation of phases that were not seen in the *ex-situ* measurements. At temperatures above ≈ 500 °C, a decrease in the peak intensities of the initial

phases is observed, accompanied by the growth of product phases. Using reported diffraction data,[39] the initial phases can be identified as primarily Sr_2CoMoO_6 (labeled A in Figure 4), with a small amount of the impurity $SrMoO_4$ (labeled B in Figure 4). At temperatures above 500 °C, the reduction of $SrMoO_4$ to $SrMoO_3$ is observed with the growth of $SrMoO_3$ peaks (labeled C in Figure 4). At temperatures above ≈ 650 °C, peaks corresponding to Sr_3MoO_6 (labeled D in Figure 4) begin to appear. Upon further heating above 750 °C, peaks for Co metal and the compounds SrO and Sr_2MoO_4 (labeled G, E, F in Figure 4, respectively) are observed. The mass fractions for each of the species, as determined using the *GSAS-II* software,[37] are plotted as a function of temperature in Figure 5. The disappearance and growth of the above phases can be described by the following chemical reactions:

$$SrMoO_4 \xrightarrow{\Delta,\ H_2} SrMoO_3 + \tfrac{1}{2}O_2 \quad (2)$$

$$2Sr_2CoMoO_6 \xrightarrow{\Delta,\ H_2} Sr_3MoO_6 + SrMoO_3 + 2Co + \tfrac{3}{2}O_2 \quad (3)$$

$$Sr_3MoO_6 \xrightarrow{\Delta,\ H_2} SrMoO_3 + 2SrO + \tfrac{1}{2}O_2 \quad (4)$$

$$SrMoO_3 + SrO \xrightarrow{\Delta,\ H_2} Sr_2MoO_4 \quad (5)$$

This series of reactions describes the initial reduction of the $SrMoO_4$ impurity to $SrMoO_3$, followed by the reduction of SCMO and formation of various strontium molybdate oxides, strontium oxide, Co metal, and oxygen vacancies. This agrees with the published phase diagram for SCMO under reducing conditions.[40] Reactions 2-4 can be correlated to the USAXS/SAXS data, in which there is very little change in the MDs and VFs of both populations at temperatures below 500 °C, where no chemical reactions occur. For population 1, the increase and then decrease in the MD between 535 °C and 697 °C corresponds to reactions 2 and 3, in which $SrMoO_4$ is reduced to $SrMoO_3$, and the reduction of SCMO to form Sr_3MoO_6, $SrMoO_3$ and Co metal has begun. The increase in MD

in this region can be attributed to the formation of oxygen vacancies and increase in pore size due to reactions 2 and 3. The following decrease in size could therefore be due to formation of the lower density Sr_3MoO_6 phase and the introduction of Sr into the previously formed pores, therefore decreasing the pore size. The second fluctuation in the MD of population 1 between 697 °C and 755 °C may then be attributed to reactions 4 and 5, in which more oxygen vacancies are formed initially, followed by densification of the material to form the final Sr_2MoO_4 phase. The decrease in the VF of population 1 corresponds to the general trend of higher density phases transforming into lower density phases with an overall reduction in pore volume during reactions 3-5, and the minor fluctuations may be attributed the changes in the pore sizes during the experiment, as described above.

For population 2, the increase and following decrease in MD between 542 °C and 723 °C may also be due to the formation of oxygen vacancies and increase in pore size due to reactions 2 and 3. At the same time, reaction 3 results in the exsolution of Co from the structure, which may cause the steady increase in diameter to 17 nm beyond 723 °C. Likewise, the steady increase in the VF of population 2 throughout the experiment may also be attributed to the growth of Co nanoparticles. The final VF of 6.1 % agrees well with that of the final Co solid mass fraction of 8.4 % determined from the WAXS data (Figure 5), when this is converted to VF. Evidence for the exsolution of Co or Ni nanoparticles has been observed in microscopy images of SCMO and SNMO, respectively, after reduction[15,17] and their precipitation at the boundaries between the grains of the bulk material has been documented in one case.[38]

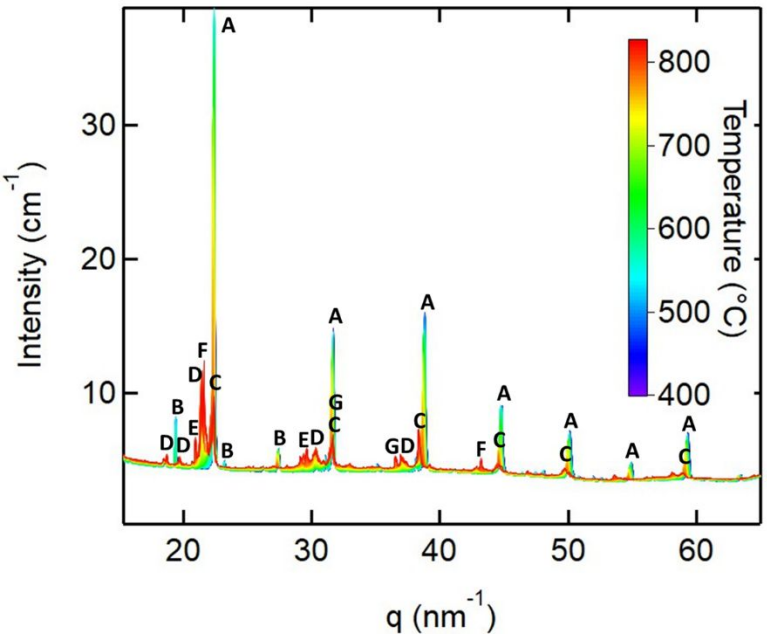

Figure 4. *In-situ* WAXS of SCMO collected from 400 °C to 825 °C under a flow of 4 % mass H_2 / 96 % mass N_2 (Sr_2CoMoO_6 (A), $SrMoO_4$ (B), $SrMoO_3$ (C), Sr_3MoO_6 (D), SrO (E), Sr_2MoO_4 (F), Co (G)). Statistical uncertainties are smaller than the line thicknesses plotted.

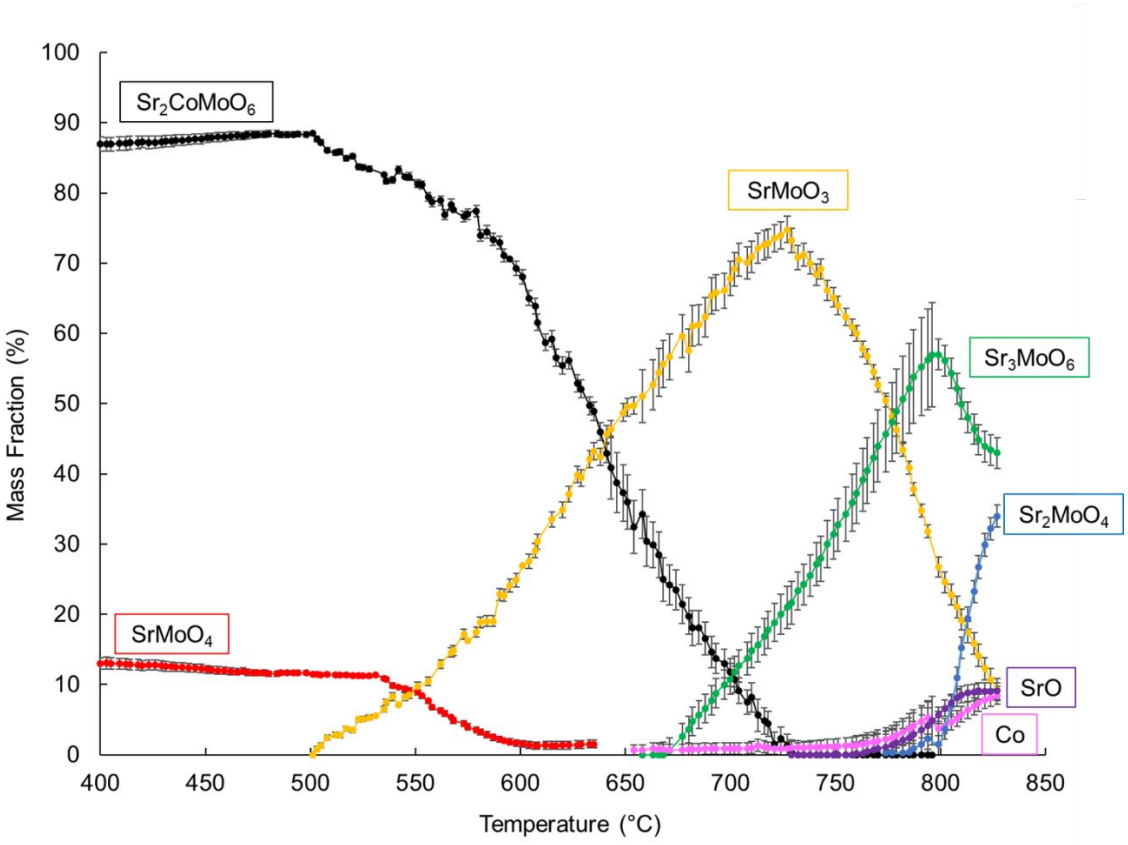

Figure 5. Phase fractions plotted as a function of temperature for the species formed during the reduction of SCMO under 4% H_2 / 96% N_2. Each phase is denoted by the following colors: Sr_2CoMoO_6 (black), $SrMoO_4$ (red), $SrMoO_3$ (orange), Sr_3MoO_6 (green), Sr_2MoO_4 (blue), SrO (purple), and Co (pink). The uncertainties in each point were calculated by the *GSAS-II* software.

In-situ conductivity measurements

In addition to the *in-situ* USAXS/SAXS/WAXS measurements, the conductivity of SCMO was also measured as a function of temperature, and the results are plotted in Figure 6. The data exhibit multiple regimes, in which there is a gradual, linear increase in conductivity between 400 °C and ≈ 550 °C, a sharp increase in conductivity between 550 °C and 720 °C, and a plateau between 720 °C and 775 °C. Between 775 °C and the final temperature of 825 °C, there is a slight decrease, then increase in the conductivity. The initial, linear regime describes the intrinsic conductivity of

the starting material, but the change in slope between 550 °C and 720 °C indicates that the material has undergone decomposition. Based on the WAXS data, reactions 2 and 3 are occurring in this temperature range, forming $SrMoO_3$, Sr_3MoO_6 and Co metal. The sharp rise in conductivity could be due to the formation of highly conductive $SrMoO_3$ and Co phases,[5,38] which plateau at a high value once the reaction is complete. The slight decrease, then increase in conductivity between 775 °C and 825 °C can be associated with the reduction of $SrMoO_3$ combined with the continued growth of Co nanoparticles. In this way, the measured conductivity can be related to the decomposition of the sample during heating. The conductivity measured here shows a similar profile to that which was reported by Zhang et. al. for the heating of SCMO over a comparable temperature range under 5 % mass H_2 / 95 % mass Ar atmosphere, although their conductivity values were slightly higher, particularly at low temperatures.[16] The reason for this may be due to differences in the initial concentration of the $SrMoO_4$ impurity between the two studies, where a higher concentration of this phase in the current work would decrease the conductivity of the sample at low temperatures. The conductivity values would then become more similar at higher temperatures as this phase is reduced. Also, a slightly lower H_2 concentration (4 % mass) was used for the gas environment in the present study, and SCMO has been shown to have lower conductivity values at lower H_2 concentrations.[14,16] The conductivity values at high temperatures (after completion of reactions 2 and 3) are similar to those measured by Huang et. al. after reduction of SCMO under 5 % mass H_2 / 95 % mass Ar atmosphere for 20 hours.[14]

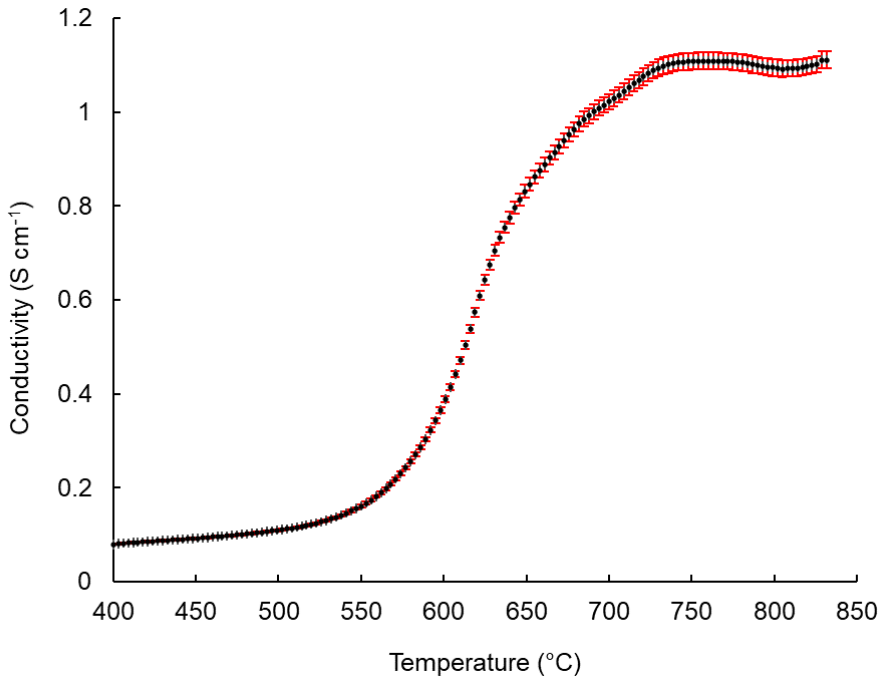

Figure 6. Temperature dependent conductivity of SCMO measured in 4 % mass H_2 / 96 % mass N_2. The uncertainties for each data point are ± 1.6 % based on the uncertainties in the sample length and area, as well as the resolution of the source/measure unit.

SEM

Ex-situ SEM was performed on the SCMO samples before and after the heat treatment under 4 % mass H_2. The images (Figure 7) show that after the heat treatment, there is an overall increase in grain size and decrease in porosity with many large globular regions, accompanied by the appearance of nanoscale particles throughout the sample (a magnified image showing these particles is shown in Figure 7c). These are likely the Co nanoparticles detected in the WAXS profile that also correspond to the growth of population 2 in the USAXS/SAXS data.[17,38] Energy-dispersive X-ray spectroscopy (EDS) analysis in the SEM confirmed the presence of Sr, Co, Mo, and O elements in the sample. Differences in composition were not observed over a large field of view, and due to the small size of the nanoparticles compared to the large interaction volume of the 15 kV electron beam, the background signal was too high to identify the elemental composition

of the nanoparticles in Figure 7c. Furthermore, the increase in grain size of the primary species can be attributed to the formation of less dense phases, as described in reactions 2-5. Based on the phase fractions determined from the WAXS data, the initial density of the primary species is ≈ 5.60 g/cm^3, and the density after reduction is ≈ 5.13 g/cm^3. A decrease in sample density is further confirmed by an increase in sample X-ray transmission (from ≈ 0.27 to ≈ 0.52) throughout the experiment. The decrease in porosity agrees with the hypothesis that the fluctuation in size observed in population 1 is predominately associated with fluctuations in pore size. As larger, less dense phases form, the pore size decreases, resulting in an observed net decrease in the MD of population 1. Therefore, the SEM observations corroborate the inferences from both the X-ray scattering data and electrical conductivity measurements.

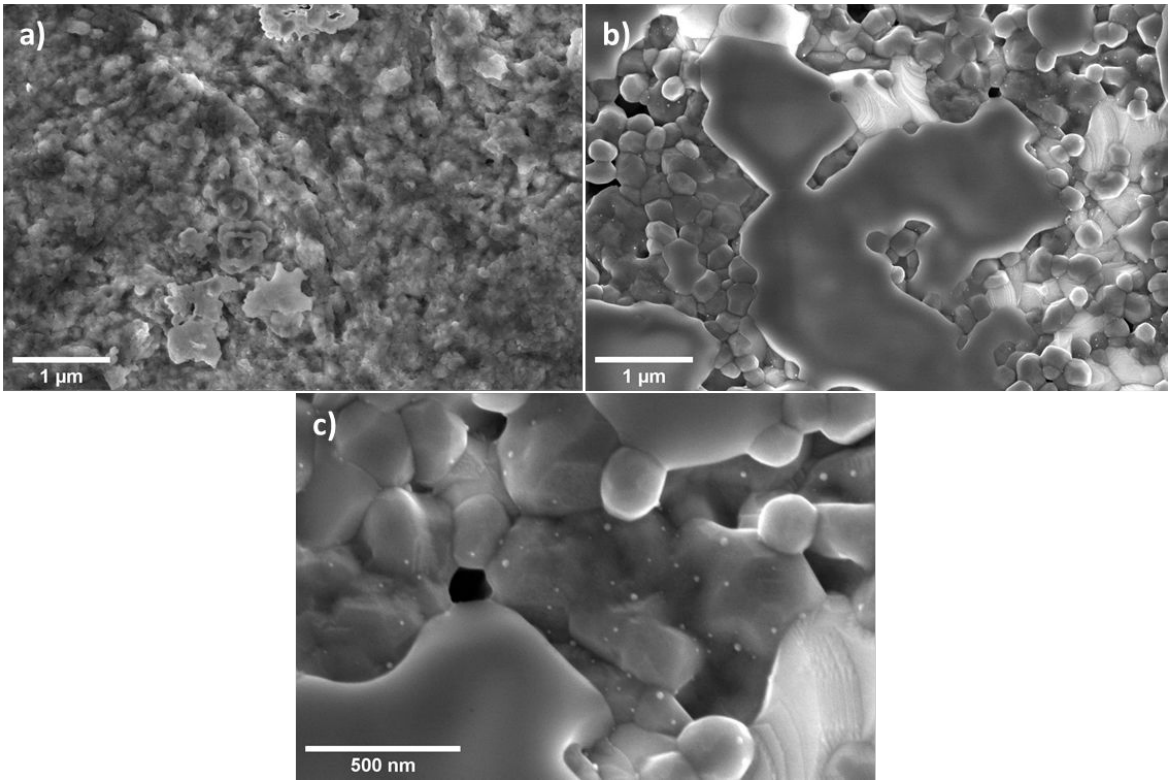

Figure 7. SEM images of the initial (a) and heat treated (b) SCMO sample. A magnified image of the heat-treated sample (c) shows the presence of nano-sized particles, which are likely Co.

CONCLUSIONS

In summary, a cell design for the simultaneous collection of USAXS/SAXS/WAXS and electrical conductivity data was developed for the *in-situ* study of SOFC electrodes. The cell allows for *in-situ* studies of a sample heated to relevant SOFC operating temperatures and for the flowing of a fuel gas. The resulting X-ray scattering and electrical conductivity data can be correlated to one another, enabling the ability to draw connections between changes in the conductivity and the microstructural and phase evolution of the sample. For the SOFC anode SCMO, continuous heating under a reducing atmosphere led to the exsolution of Co from the double perovskite structure, formation of new strontium molybdate phases, and a sharp rise in conductivity. Fitting a two-population model to the USAXS/SAXS data revealed an ≈ 5 % reduction in the VF accompanied by a decrease from 550 nm to 464 nm in the MD of population 1, indicating a decrease in pore size. For population 2, the VF and MD steadily increased to the final values of 6.1 % and 17 nm, respectively, which was attributed to the growth of Co nanoparticles. The fluctuations in the VFs and MDs of both populations can be correlated to the WAXS data, in which new phases of various densities develop over time. Namely, the growth of a Co phase with a final mass percentage of 8.4 % was observed. This agrees well with the final solid VF of 6.1 % from the USAXS/SAXS fitting for population 2, when converting the mass percentage to VF. Additionally, a sharp rise in conductivity between 550 °C and 720 °C corresponded to the formation of the highly conductive Co and $SrMoO_3$ phases detected in the WAXS data. These observations were further corroborated by microscopy analysis of the initial and final samples, in which SEM images showed an increase in primary-feature grain size, a decrease in porosity and the formation of nano-sized particles. Future studies aim to use this cell design to conduct similar

experiments on other materials relevant to the SOFC industry under a variety of fuel gasses, such as methane.

ASSOCIATED CONTENT

Supporting Information

The following files are available free of charge.

A PDF containing details of the electrical cell assembly as well as the X-ray densities and scattering contrast factors of the materials used in this study.

AUTHOR INFORMATION

Corresponding Author

*Corresponding email: switt@fraunhofer.org

Present Addresses

[§]Fraunhofer USA, Inc. Center for Coatings and Diamond Technologies, East Lansing, MI 48824, USA

Author Contributions

The manuscript was written through contributions of all authors. All authors have given approval to the final version of the manuscript.

Notes

[†]Certain commercial materials and equipment are identified in this paper only to specify adequately the experimental procedure. In no case does such identification imply recommendation

by NIST nor does it imply that the material or equipment identified is necessarily the best available for this purpose.

‡The mass percentage of hydrogen in the gas mixture used during *in-situ* experiments was lower than that which was used during *ex-situ* sample treatment due to heightened safety requirements at the X-ray beamline.

ACKNOWLEDGEMENT

Financial support for this work was provided by the U.S. National Institute of Standards and Technology. This research used resources of the Advanced Photon Source, a U.S. Department of Energy (DOE) Office of Science User Facility operated for the DOE Office of Science by Argonne National Laboratory under Contract No. DE-AC02-06CH11357. USAXS/SAXS/WAXS data were collected at APS sector 9-ID operated by Argonne National Laboratory's X-ray Science Division (XSD).

We would also like to thank Dr. Russell Maier and Dr. Andrew Herzing for providing their expertise during technical discussions related to the work, Dr. Megan Butala for assistance with the *GSAS-II* software, and Dr. Andrei Kolmakov for supplying the Silver Conductive Epoxy used to mount the samples.

REFERENCES

1. Goodenough, J. B.; Huang, Y. H. Alternative anode materials for solid oxide fuel cells. *J. Power Sources* **173**, 1–10 (2007).

2. da Silva, F. S.; de Souza, T. M. Novel materials for solid oxide fuel cell technologies: A literature review. *Int. J. Hydrogen Energy* **42**, 26020–26036 (2017).

3. Zhang, Q.; Wei, T.; Huang, Y. H. Electrochemical performance of double-perovskite Ba_2MMoO_6 (M = Fe, Co, Mn, Ni) anode materials for solid oxide fuel cells. *J. Power Sources* **198**, 59–65 (2012).

4. Huang, Y.-H.; Dass, R. I.; Xing, Z.-L.; Goodenough, J. B. Double Perovskites as Anode Materials for Solid-Oxide Fuel Cells. *Science* **2**, 254–258 (2006).

5. dos Santos-Gómez, L.; León-Reina, L.; Porras-Vázquez, J. M.; Losilla, E. R.; Marrero-López, D. Chemical stability and compatibility of double perovskite anode materials for SOFCs. *Solid State Ionics* **239**, 1–7 (2013).

6. Huang, Y.-H.; Dass, R. I.; Denyszyn, J. C.; Goodenough, J. B. Synthesis and Characterization of $Sr_2MgMoO_{6-\delta}$. *J. Electrochem. Soc.* **153**, A1266 (2006).

7. Li, C.; Wang, W.; Zhao, N.; Liu, Y.; He, B.; Hu, F.; Chen, C. Structure properties and catalytic performance in methane combustion of double perovskites $Sr_2Mg_{1-x}Mn_xMoO_{6-\delta}$. *Appl. Catal. B Environ.* **102**, 78–84 (2011).

8. Marrero-López, D.; Peña-Martínez, J.; Ruiz-Morales, J. C.; Pérez-Coll, D.; Aranda, M. A. G.; Núñez, P. Synthesis, phase stability and electrical conductivity of $Sr_2MgMoO_{6-\delta}$ anode. *Mater. Res. Bull.* **43**, 2441–2450 (2008).

9. Niu, B.; Jin, F.; Fu, R.; Feng, T.; Shen, Y.; Liu, J.; He, T. Pd-impregnated $Sr_{1.9}VMoO_{6-\delta}$ double perovskite as an efficient and stable anode for solid-oxide fuel cells operating on sulfur-containing syngas. *Electrochim. Acta* **274**, 91–102 (2018).

10. Xiao, G.; Liu, Q.; Dong, X.; Huang, K.; Chen, F. $Sr_2Fe_{4/3}Mo_{2/3}O_6$ as anodes for solid oxide fuel cells. *J. Power Sources* **195**, 8071–8074 (2010).

11. Liu, Q.; Dong, X.; Xiao, G.; Zhao, F.; Chen, F. A novel electrode material for symmetrical SOFCs. *Adv. Mater.* **22**, 5478–5482 (2010).

12. Wang, Z.; Tian, Y.; Li, Y. Direct CH_4 fuel cell using Sr_2FeMoO_6 as an anode material. *J. Power Sources* **196**, 6104–6109 (2011).

13. Zhang, L.; Zhou, Q.; He, Q.; He, T. Double-perovskites $A_2FeMoO_{6-\delta}$(A = Ca, Sr, Ba) as anodes for solid oxide fuel cells. *J. Power Sources* **195**, 6356–6366 (2010).

14. Huang, Y.-H.; Liang, G.; Croft, M.; Lehtimäki, M.; Karppinen, M.; Goodenough, J. B. Double-Perovskite Anode Materials Sr_2MMoO_6 (M = Co, Ni) for Solid Oxide Fuel Cells. *Chem. Mater.* **21**, 2319–2326 (2009).

15. Tan, W.; Pan, C.; Yang, S.; Zhong, Q. Application of symmetric solid oxide fuel cell in fuel containing sulfur: I. Effect of electrodes. *J. Power Sources* **277**, 416–425 (2015).

16. Zhang, P.; Huang, Y. H.; Cheng, J. G.; Mao, Z. Q.; Goodenough, J. B. Sr_2CoMoO_6 anode for solid oxide fuel cell running on H_2 and CH_4 fuels. *J. Power Sources* **196**, 1738–1743 (2011).

17. Gwan, M. A.; Yun, J. W. Carbon tolerance effects of $Sr_2NiMoO_{6-\delta}$ as an alternative anode in solid oxide fuel cell under methane fuel condition. *J. Electroceramics* **40**, 171–179 (2018).

18. Presto, S.; Kumar, P.; Varma, S.; Viviani, M.; Singh, P. Electrical conductivity of NiMo–based double perovskites under SOFC anodic conditions. *Int. J. Hydrogen Energy* **43**, 4528–4533 (2018).

19. Wei, T.; Ji, Y.; Meng, X.; Zhang, Y. $Sr_2NiMoO_{6-\delta}$ as anode material for $LaGaO_3$-based solid

oxide fuel cell. *Electrochem. commun.* **10**, 1369–1372 (2008).

20. Mcbreen, J.; O'Grady, W. E.; Pandya, K. I.; Hoffman, R. W.; Sayers, D. E. EXAFS Study of the Nickel Oxide Electrode. *Langmuir* **3**, 428–433 (1987).

21. Melroy, O. R.; Samant, M. G.; Borges, G. L.; Gordon, II, J. G. In-Plane Structure of Underpotentially Deposited Copper on Gold (111) Determined by Surface EXAFS. *Langmuir* **4**, 728–732 (1988).

22. Binninger, T.; Fabbri, E.; Patru, A.; Garganourakis, M.; Han, J.; Abbot, D. F.; Sereda, O.; Kotz, R.; Menzel, A.; Nachtegaal, M.; Schmidt, T. J. Electrochemical Flow-Cell Setup for In Situ X-ray Investigations I. Cell for SAXS and XAS at Synchrotron Facilities. *J. Electrochem. Soc.* **163**, 906–912 (2016).

23. Borkiewicz, O. J.; Shyam, B.; Wiaderek, K. M.; Kurtz, C.; Chupas, P. J.; Chapman, K. W. The AMPIX electrochemical cell: A versatile apparatus for in situ X-ray scattering and spectroscopic measurements. *J. Appl. Crystallogr.* **45**, 1261–1269 (2012).

24. Ocko, B. M.; Wang, J.; Davenport, A.; Isaacs, H. In Situ X-Ray Reflectivity and Diffraction Studies on the Au(001) Reconstruction in an Electrochemical Cell. *Phys. Rev. Lett.* **65**, 1466–1470 (1990).

25. Herron, M. E.; Doyle, S. E.; Pizzini, S.; Roberts, K. J.; Robinson, J.; Hards, G.; Walsh, F. C. In situ studies of a dispersed platinum on carbon electrode using X-ray absorption spectroscopy. *J. Electroanal. Chem.* **324**, 243–258 (1992).

26. Haubold, H.-G.; Wang, X. H.; Jungbluth, H.; Goerigk, G.; Schilling, W. In situ anomalous small-angle X-ray scattering and X-ray absorption near-edge structure investigation of

catalyst structures and reactions. *J. Mol. Struct.* **383**, 283–289 (1996).

27. Roth, C.; Martz, N.; Buhrmester, T.; Scherer, J.; Fuess, H. In-situ XAFS fuel cell measurements of a carbon-supported Pt–Ru anode electrocatalyst in hydrogen and direct methanol operation. *Phys. Chem. Chem. Phys.* **4**, 3555–3557 (2002).

28. Braun, A.; Shrout, S.; Fowlks, A. C.; Osaisai, B. A.; Seifert, S.; Granlund, E.; Cairns, E. J. Electrochemical in situ reaction cell for X-ray scattering, diffraction and spectroscopy. *J. Synchrotron Radiat.* **10**, 320–325 (2003).

29. Wiltshire, R. J. K.; King, C. R.; Rose, A.; Wells, P. P.; Hogarth, M. P.; Thompsett, D.; Russell, A. E. A PEM fuel cell for in situ XAS studies. *Electrochim. Acta* **50**, 5208–5217 (2005).

30. Hirayama, M.; Sonoyama, N.; Ito, M.; Minoura, M.; Mori, D.; Yamada, A.; Tamura, K.; Mizuki, J.; Kanno, R. Characterization of Electrode/Electrolyte Interface with X-Ray Reflectometry and Epitaxial-Film $LiMn_2O_4$ Electrode. *J. Electrochem. Soc.* **154**, A1065–A1072 (2007).

31. Petrova, O.; Kulp, C.; van den Berg, M. W. E.; Klementiev, K. V; Otto, B.; Otto, H.; Lopez, M.; Bron, M.; Grünert, W. A spectroscopic proton-exchange membrane fuel cell test setup allowing fluorescence x-ray absorption spectroscopy measurements during state-of-the-art cell tests. *Rev. Sci. Instrum.* **82**, 1–8 (2011).

32. Vasala, S.; Lehtimäki, M.; Huang, Y. H.; Yamauchi, H.; Goodenough, J. B.; Karppinen, M. Degree of order and redox balance in B-site ordered double-perovskite oxides, $Sr_2MMoO_{6-\delta}$ (M=Mg, Mn, Fe, Co, Ni, Zn). *J. Solid State Chem.* **183**, 1007–1012 (2010).

33. Ilavsky, J.; Zhang, F.; Andrews, R. N.; Kuzmenko, I.; Jemian, P. R.; Levine, L. E.; Allen, A. J. Development of combined microstructure and structure characterization facility for in situ and operando studies at the advanced photon source. *J. Appl. Crystallogr.* **51**, 867–882 (2018).

34. Allen, A. J.; Ilavsky, J.; Braun, A. Multi-scale Microstructure Characterization of Solid Oxide Fuel Cell Assemblies With Ultra Small-Angle X-Ray Scattering. *Adv. Eng. Mater.* **11**, 495–501 (2009).

35. Allen, A. J.; Ilavsky, J.; Jemian, P. R.; Braun, A. Evolution of electrochemical interfaces in solid oxide fuel cells (SOFC): a Ni and Zr resonant anomalous ultra-small-angle X-ray scattering study with elemental and spatial resolution across the cell assembly. *RSC Adv.* **4**, 4676–4690 (2014).

36. Ilavsky, J.; Jemian, P. R. Irena: Tool suite for modeling and analysis of small-angle scattering. *J. Appl. Crystallogr.* **42**, 347–353 (2009).

37. Toby, B. H.; Von Dreele, R. B. GSAS-II: The genesis of a modern open-source all purpose crystallography software package. *J. Appl. Crystallogr.* **46**, 544–549 (2013).

38. Graves, C.; Sudireddy, B. R.; Mogensen, M. Molybdate Based Ceramic Negative-electrode Materials for Solid Oxide Cells. *ECS Trans.* **28**, 173–192 (2010).

39. NIST Inorganic Crystal Structure Database, NIST Standard Reference Database Number 3, National Institute of Standards and Technology. http://www.nist.gov/mml/csd/informatics_research/srsw.cfm (2014) doi:https://doi.org/10.18434/M32147.

40. Sereda, V. V.; Tsvetkov, D. S.; Sednev, A. L.; Druzhinina, A. I.; Malyshkin, D. A.; Zuev, A. Y. Thermodynamics of Sr_2NiMoO_6 and Sr_2CoMoO_6 and their stability under reducing conditions. *Phys. Chem. Chem. Phys.* **20**, 20108–20116 (2018).

41. Hayes, J. R.; Grosvenor, A. P. An investigation of the Fe and Mo oxidation states in $Sr_2Fe_{2-x}Mo_xO_6$ ($0.25 < x < 1.0$) double perovskites by X-ray absorption spectroscopy. *J. Alloys Compd.* **537**, 323–331 (2012).

42. Lindén, J.; Yamamoto, T.; Karppinen, M.; Yamauchi, H.; Pietari, T. Evidence for valence fluctuation of Fe in Sr_2FeMoO_{6-w} double perovskite. *Appl. Phys. Lett.* **76**, 2925–2927 (2000).

43. Taguchi, M.; Matsui, F.; Maejima, N.; Matsui, H.; Daimon, H. Disorder and mixed valence properties of Sr_2FeMoO_6 studied by photoelectron diffraction and x-ray absorption spectroscopy. *Surf. Sci.* **683**, 53–56 (2019).

44. Kapusta, C.; Riedi, P. C.; Zajac, D.; Sikora, M.; Teresa, J. M. De; Morellonc, L.; Ibarra, M. R. NMR study of double perovskite Sr_2FeMoO_6. *J. Magn. Magn. Mater.* **242–245**, 701–703 (2002).

For Table of Contents Only